A Simulation Study on von Karman Vortex Shedding with Navier-Stokes and Shallow-Water Models

Shin-Jye Liang[1], Shih-Huang Wu[1], Wei-Ting Chao[2,*]

[1]Department of Marine Environmental Informatics, National Taiwan Ocean University, Keelung, Taiwan

[2]Center of Excellence for Ocean Engineering, National Taiwan Ocean University; Keelung, Taiwan

Abstract

This study aims to investigate the advantages of employing numerical models based on Shallow-water equations for simulating von Karman vortex shedding. Furthermore, a comparative analysis with Navier-Stokes equations will be conducted to assess their effectiveness. In addition to Reynolds number (Re), Froude number (Fr), relevant to water depth, plays an important role in the Shallow-Water modeling of the von Karman vortex. In this study, simulations of 2D von Karman vortex shedding are performed using the Navier-Stokes model and Shallow-Water model, employing the least-squares finite-element method for space discretization and θ-method for time integration. The computed vortices characteristics, including the recirculation zone behind the cylinder, vortices size, and frequency, are presented. In the Navier-Stokes modeling, the computed results indicate that the size of vortices in space decreases and the Strouhal number increases as Re increases. In the Shallow-Water modeling for the same Re condition, the size of vortices increases and the Strouhal number decreases as Fr increases.

1. Introduction

von Karman vortex shedding, pairs of periodic counter-rotating vortices downstream of an obstacle, is generated by the flow past an obstacle, which is a classic flow mechanic problem with many engineering and science applications [1]. These flows are characterized by flow separation and vortex shedding phenomena due to the pressure gradient. This fascinating fluid mechanic problem usually occurs when the flow passes an obstacle in a specific range of Reynolds number (Re) i.e., $46 < Re < 800$ [2-3]. Different flow properties (i.e., different Re) may lead to distinct bluff body wakes. von Karman vortex shedding has been experimentally [4-8] and numerically [9-15] studied in previous studies. Real-world observations of von Karman vortex street from a circular cylinder and its effects can be found in hydrodynamic applications and engineering structures like bridges, chimneys, and skyscrapers. An excellent overview of flow past a circular cylinder can be found in Zdravkovich [16-17].

Many models have been developed with different numerical methods for incompressible viscous flows and free-surface flows [18-20]. The importance of vortex shedding and evolution in the design of submerged structures has been revealed by numerous researchers, Ai et al. [21] employed a second-order flux-limiter method to study the vortex shedding and evolution induced by the interactions between a solitary wave and a submerged horizontal plate. Their results provide a better description of the vortex generation and evolution.

A wind turbine blade is the core component of a wind turbine, the airfoil is in the low Re flow field, and the flow field instability is significantly higher than that of medium and high Re. Chang et al. [22] have numerically studied the shedding vortex characteristics of NACA 0012 airfoil at low Re. Wind-induced vibration is often used in piezoelectric energy harvesters

---

to convert wind energy into electrical energy. Li et al. [23] have developed efficient vortex-induced, wake-induced, flutter-induced, and galloping-induced wind energy harvesters. In this study, the 2D Navier-Stokes model and Shallow-Water model are used to simulate 2D von Karman vortex shedding. The models employ the least-squares finite-element approach for space discretization with the θ-method for time integration [24-25]. The Shallow-Water model has been successfully applied to model the ocean circulation of Dongsha water by Liang et al. [26].

This study aims to perform a series of simulations of 2D von Karman vortex shedding with the Navier-Stokes model and Shallow-Water model at Re of 60, 100, and 200, as well as Froude number (*Fr*) of 0.014, 0.010, and 0.007, corresponding to water depth (*h*) of 0.2, 0.4, and 0.8 m, respectively. The objective is to investigate the effect of *Re* and *Fr* on the computed results. The simulations are carried out for a long time to ensure that adequate observation of the flow characteristics is obtained. Sequential changes of flow pattern at a particular *Re* due to a change in water depth are presented. Emphasis is given to the flow wake pattern in space and the period of the vortex shedding in time. Several important flow characteristics such as the recirculation zone behind the cylinder, size of vortices, and Strouhal number (*St*), are examined with the flow conditions (input parameters). Based on the computed results, a relationship between *St* and *Re* is evaluated and compared with the previous study [16]. Moreover, the effect of *Fr* on the *St-Re* relationship of Shallow-Water modeling is discussed.

2. Governing Equations and Numerical Methods

The governing equations for the Navier-Stokes model and the Shallow-Water model are briefly presented in Section 2.1, and the numerical methods of the models are described in Section 2.2.

2.1. *Navier-Stokes equations and Shallow-Water equations*

Navier-Stokes equations are derived from the principles of mass conversation and momentum conversation, they describe how the velocity and pressure of a moving fluid are related. The 2D equations of incompressible fluids can be presented as

$$\frac{\partial u}{\partial x} + \frac{\partial v}{\partial y} = 0 \tag{1}$$

$$\frac{\partial u}{\partial t} + u\frac{\partial u}{\partial x} + v\frac{\partial u}{\partial y} = -\frac{1}{\rho}\frac{\partial p}{\partial x} + v\left(\frac{\partial^2 u}{\partial x^2} + \frac{\partial^2 u}{\partial y^2}\right) \tag{2}$$

$$\frac{\partial v}{\partial t} + u\frac{\partial v}{\partial x} + v\frac{\partial v}{\partial y} = -\frac{1}{\rho}\frac{\partial p}{\partial y} + v\left(\frac{\partial^2 v}{\partial x^2} + \frac{\partial^2 v}{\partial y^2}\right) \tag{3}$$

where *u* and *v* are flow velocity components in the *x* and *y* directions, *t* is time, ρ is the density of water, *p* is pressure, and v is the kinematic viscosity of the water.

2D Shallow-Water equations are derived by depth-integrating the 3D Navier-Stokes equations with the Leibniz integral rule. It simplifies the 3D problem to a 2D one and includes the consideration of time-varying free-surface and bottom variations.

$$\frac{\partial \eta}{\partial t} + \frac{\partial (HU)}{\partial x} + \frac{\partial (HV)}{\partial y} = 0 \tag{4}$$

$$\frac{\partial U}{\partial t} + U\frac{\partial U}{\partial x} + V\frac{\partial U}{\partial x} = -g\frac{\partial \eta}{\partial x} + S_U \tag{5}$$

$$\frac{\partial V}{\partial t} + U\frac{\partial V}{\partial x} + V\frac{\partial V}{\partial x} = -g\frac{\partial \eta}{\partial y} + S_V \tag{6}$$

where *U* and *V* are the depth-averaged velocities, which can be expressed by

$$U = \frac{1}{H} \int_{-h}^{\eta} u\, dz \tag{7}$$

$$V = \frac{1}{H} \int_{-h}^{\eta} v\, dz \tag{8}$$

$\eta(x, y, t)$ is the free surface, $h(x, y)$ is the bottom elevation, and $H = \eta - h$ is the total water depth. S_U and S_V are the source terms, including the atmosphere pressure, wind stress, bottom drag stresses, etc. The Shallow-Water equations are derived by depth-integrating the 3D NS equations with the hydrostatic assumption by the Leibnitz rule. These equations are represented by Eqs. (4)-(6).

2.2. Numerical methods

Both the Navier-Stokes model and the Shallow-Water model are formulated with the least-squares finite-element approach [27-28]. The θ-method is employed for the time integration. Due to the use of least-squares formulation, the resulting system of equations in both models is symmetric and positive-definite. Therefore, an efficient solution can be obtained by using preconditioned conjugate gradient solver [29]. The detailed formulation of the Shallow-Water model with source terms as well as verifications and application of the model can be found in [24-25].

3. Results and Discussion

The study problem which involves the modeling of von Karman vortices in various Re and water depth (H), is briefly described. This study presents the modeling results of the Navier-Stokes and Shallow-Water models. Additionally, the computed results are compared with the results of the previous study. Finally, the impact of Re and h on the size of vortices and St is discussed.

3.1. Study problem

The domain of the simulation is defined as -4.0 m <= X <= 20.0 m in the *x* direction and -4.0 m <= Y <= 4.0 m in the *y* direction, as shown in Fig. 1. A circular cylinder with a diameter $D = 1.0$ m and the center locates at the origin. An inflow with a constant speed $U = 0.01$ m/s enters the domain from the left boundary, passes the cylinder, and exits the domain from the right open boundary. The free slip boundary condition is employed for both top and bottom boundaries, while the non-slip boundary condition is enforced on the cylinder boundary. von Karman vortex shedding is modeled in the present study using three Re conditions, i.e., $Re = 60$, 100, and 200. Point P is the location of the monitor point where flow variations are recorded for the post-process and analysis.

In addition, Fig. 1 depicts the computational meshes, a total of 5,093 9-node quadrilaterals, and 20,590 nodes. Finer meshes are used near the cylinder area because a significant variation of flow and wave in that area is expected. $\Delta t = 0.05$ s is used in the computations. The simulation begins with a motionless flow, i.e., fluid initially rests. Throughout the transition, i.e., about 3-5 periods of von Karman vortex shedding, depending on the value of Re. The flow develops and reaches a periodic state in both space and time.
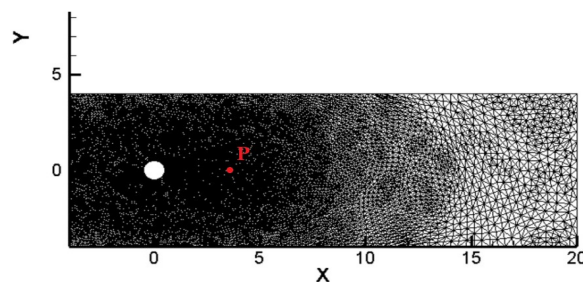

Fig. 1 Illustration of the study problem, domain, and computational meshes

3.2. Navier-Stokes modeling results

Characteristics of vortex shedding are more prominent in the cross direction compared to the mainstream direction. Therefore, the velocity component in the *y*-direction is chosen to illustrate the spatial variations of vortex shedding at various *Re*. Fig. 2 plots *V*-Contours of Navier-Stokes modeling at different *Re*. It is noted that the recirculation zone, about 1.5-2.5 *D*, becomes smaller as *Re* increases. As *Re* increases, the pattern of the vortex streets becomes more organized, and the size of the vortices in the span (mainstream) direction decreases.
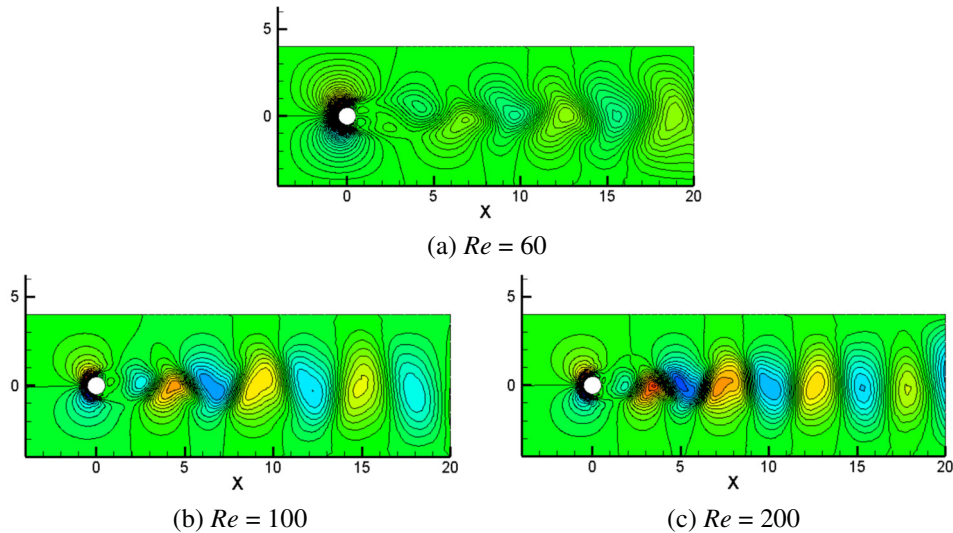
(a) *Re* = 60

(b) *Re* = 100   (c) *Re* = 200

Fig. 2 *V*-Contours of Navier-Stokes modeling with *Re*

Fig. 3 shows the time history of *U* and *V* at monitor point P for different *Re*. It is observed that flow reaches the periodic state with varying periods of transition. About 3-5 periods of von Karman vortex shedding. The frequency of *U* is observed to be twice that of *V*, which is a typical feature of the von Karman vortex shedding. *St* (Strouhal number), which associates the frequency of the von Karman vortex shedding is computed by $St = fL / U$, where *L* and *U* are reference length and velocity, and *f* is the frequency of *V*. Computed *St* are 0.142, 0.163, and 0.184 for *Re* = 60, 100, and 200, respectively. The data shows that *St* increases as *Re* increases, and the momentum becomes more significant, resulting in faster variations of the vortices.
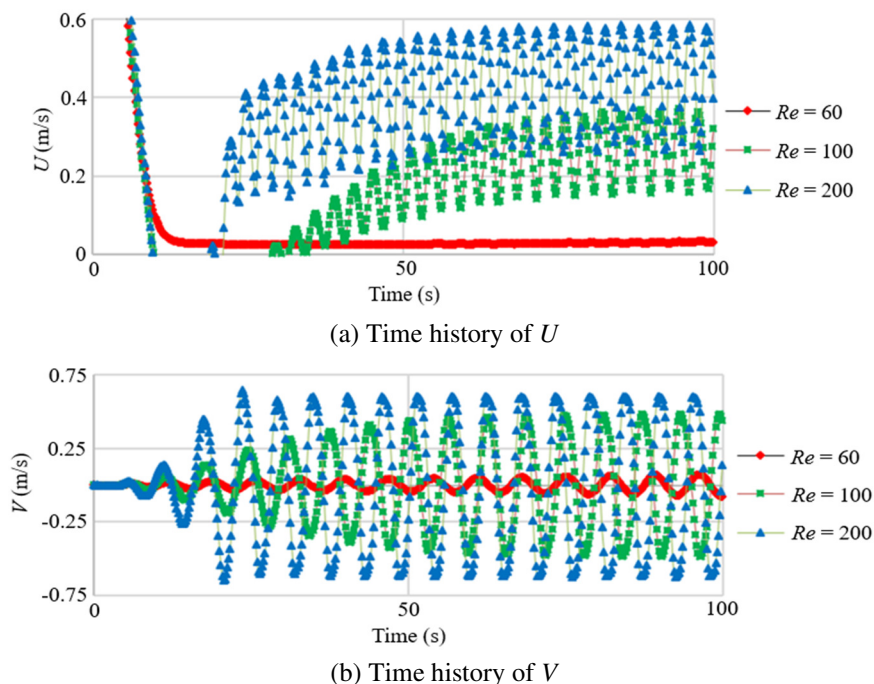
(a) Time history of *U*

(b) Time history of *V*

Fig. 3 Time history of *U* and *V* in Navier-Stokes modeling of *Re* = 60, 100, and 200

3.3. Shallow-Water modeling results

Fig. 4 depicts the time history of *U* and *V* of the Shallow-Water modeling with *h* = 0.8 m and *Re* = 60, 100, and 200, respectively. As mentioned previously, the variation of *V* is more significant than that of *U*. It is evident that the frequency of *U* is approximately twice that of *V*, which is another salient feature of vortex shedding. Furthermore, the frequency of the von Karman vortex shedding increases the rise of *Re*. The main reason for this observation is that the momentum becomes much more significant as *Re* increases. This leads to faster variations of the vortices, as illustrated in Fig. 2.
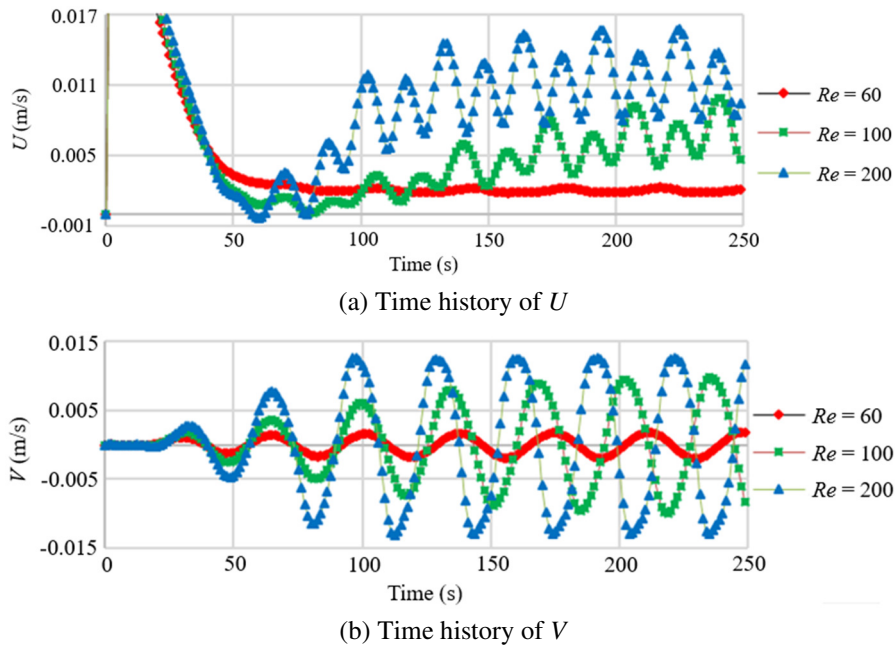
(a) Time history of *U*

(b) Time history of *V*

Fig. 4 Time history of *U* and *V* in Shallow-Water modeling with *h* = 0.8 m of *Re* = 60, 100, and 200

(a) Time history of *U*
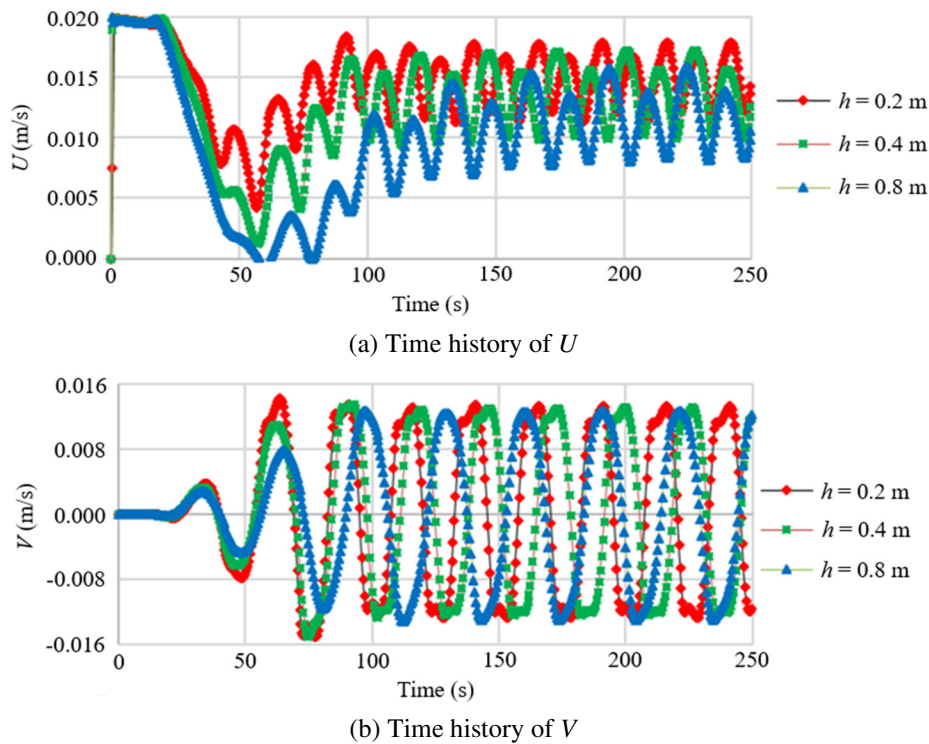
(b) Time history of *V*

Fig. 5 Time history of *U* and *V* in Shallow-Water modeling of *Re* = 200 with *h* = 0.2, 0.4, and 0.8 m

Water depth, expressed by *Fr*, also affects the temporal and spatial variation of vortex shedding. Fig. 5 illustrates the time history of *U* and *V* of the Shallow-Water modeling with *Re* = 200 and *h* = 0.2, 0.4, and 0.8 m, respectively. The periodicity of *V* is more distinct than that of *U*. The flow reaches a stationary state with different periods of transition at different water

depths. As the water depth decreases, the period of flow transition becomes shorter. It reveals that the frequency of von Karman vortex shedding increases as *h* decreases. In other words, the smaller the inertia, the faster the fluid responds to the inflow forcing as the water depth decreases.

Well-organized flow oscillations downstream the cylinder are the most prominent phenomenon of the von Karman vortex shedding, especially the variations of *V*. Fig. 6 plots *V*-contours of von Karmann vortex shedding by the Navier-Stokes and Shallow-Water modelings with *Re* = 60, 100, and 200 and *h* = 0.2, 0.4, and 0.8 m, respectively. It should be noted that no appropriate solution is obtained with *Re* = 60 with *h* = 0.2 m due to the influence of the top and bottom walls. The interactions between the sidewall vortices and cylinder vortices indicate that the computational domain needs to be more significant to accommodate considered the flow condition. Flow property, especially the *V*-contours, exhibit significant variation with different *Re* and *h*. Flow becomes more complicated as *Re* increases. It is observed that the recirculation zone behind the cylinder, about 2.0-3.5 *D*, decreases as *Re* increases, and the vortices structure becomes periodic in space with a size of about 1.5-2.5 *D* in the span direction downstream of the cylinder.
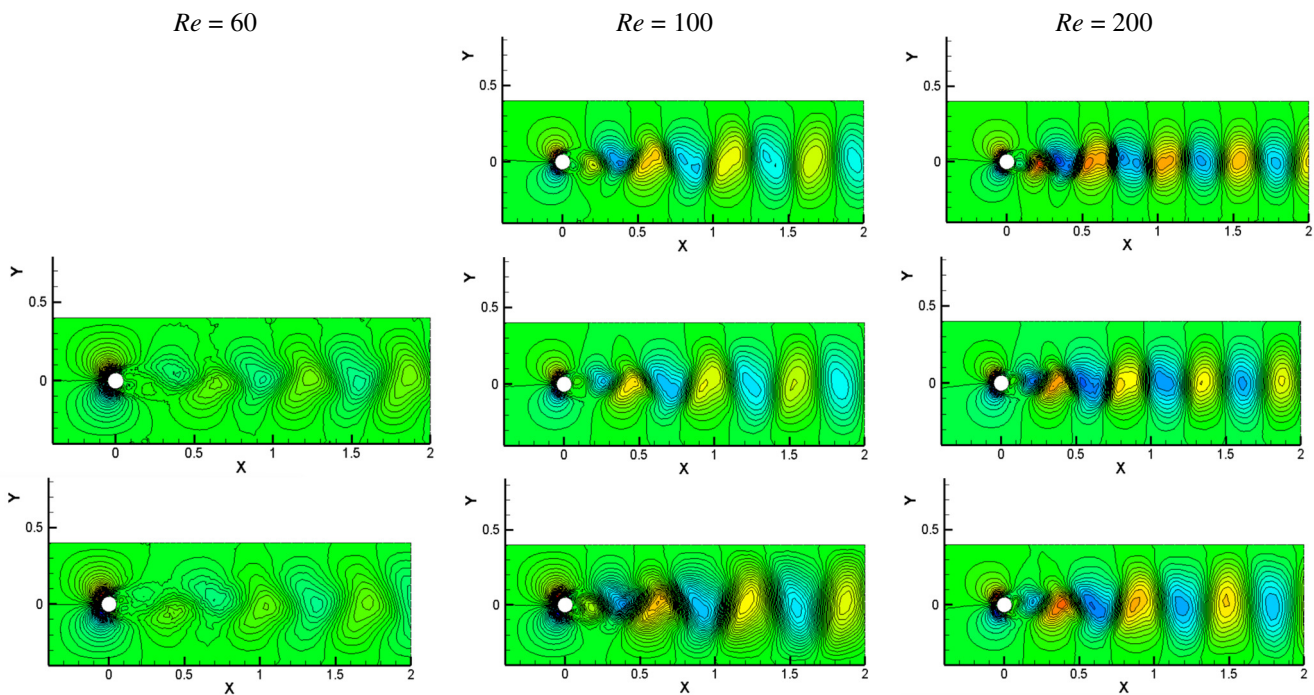

Fig. 6 Comparison of *V*-contours in Shallow-Water modeling of *Re* = 60, 100, and 200

3.4. Discussions

The Navier-Stokes model is based on the 2D Navier-Stokes equations, Eqs. (1)-(3), are simplified from the 3D Navier-Stokes equations by neglecting the vertical (*z*) related terms. While the Shallow-Water model is based on the Shallow-Water equations, Eqs. (4)-(6), is derived by vertically integrating the 3D Navier-Stokes equations with the hydrostatic assumption and including the boundary conditions of the free surface and bottom using the Leibniz rule. The pressure gradient terms in Eqs. (2)-(3) are replaced by the gradients of the free surface in Eqs. (5)-(6). Therefore, water depth $H(x, y, t) = \eta(x, y, t) - h(x, y)$ plays an important role in determining the flow properties of the free surface. The effect of *h* is evaluated and expressed by the *Fr*, i.e., $Fr = U/\sqrt{gH}$. In addition, the required minimum domain is found to be dependent on *Re* and *h*, as well as the applied boundary conditions.

Computed results of von Karmann vortices by the Navier-Stokes model and Shallow-Water model are summarized and shown with the previous study in Fig. 7. Predicted relationship of *St* vs. *Re* of the Navier-Stokes modeling shows a good agreement and similar trend [12, 30]. Water depth has a pronounced effect on the temporal oscillations of the vortices. *St*

decreases as *Fr* decreases, i.e., the vortices oscillate slower as the water depth increases, for the same *Re*. The reason for this observation is attributed to more volume and inertia of fluid as water depth increases retards the response of the fluid to the inflow forcing.
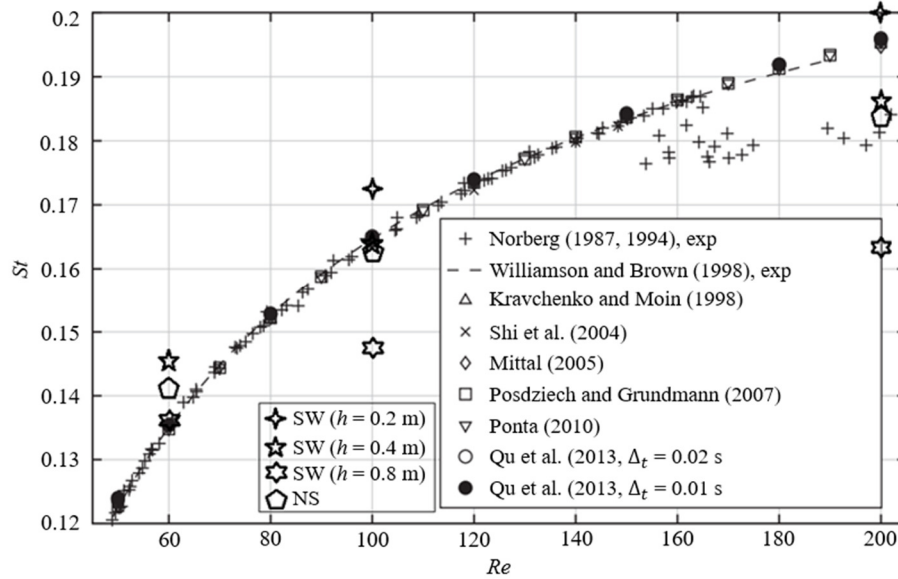

Fig. 7 Comparison of computed *St-Re* relationship with the previous study

Note: Background figure is from Qu et al. [12]
Cross marks (x) denote the results of the Navier-Stokes modeling.
Star marks (★) denote the results of Shallow-Water modeling.

4. Conclusions

A 2D von Karman vortex shedding due to flow passing a stationary circular cylinder was simulated in this study using the Navier-Stokes and Shallow-Water models under various *Re* and *Fr* conditions. The computed vortices characteristics, including the recirculation zone behind the cylinder, vortices size, and frequency of the vortices, were investigated. The main conclusions are summarized as:

(1) Computed results show that cylinder vortices are periodic both in space and time, and their structures and variations become more complicated as *Re* increases.

(2) Computed results of the Navier-Stokes modeling show that the recirculation zone behind the cylinder, approximately 3.0-5.0 *D*, and the spatial size of the vortices, about 1.5-2.5 *D* in the span direction, decreases as *Re* increases. The computed Strouhal number (*St*) agrees with the previous study.

(3) Simulations of the Shallow-Water modeling show that water depth, related to *Fr*, plays an important role in the vortices properties. The larger the water depth, the smaller the recirculation zone, and the larger the size of the vortices for the same *Re* condition.

(4) *St* is found to be very sensitive to the water depth: the smaller *St*, implying a longer period of vortex shedding, the larger the water depth for the same *Re* condition.

It is noted that the required minimum domain, water depth, and applied boundary conditions for different flows deserve further study in the future.

Conflicts of Interest

The authors declare no conflict of interest.

References

[1] R. King, "A Review of Vortex Shedding Research and Its Application," Ocean Engineering, vol. 4, no. 3, pp. 141-171, July 1977.

[2] C. H. K. Williamson, "Vortex Dynamics in the Cylinder Wake," Annual Review of Fluid Mechanics, vol. 28, pp. 477-539, January 1996.

[3] M. Heil, J. Rosso, A. L. Hazel, and M. Brøns, "Topological Fluid Mechanics of the Formation of the Kármán-Vortex Street," Journal of Fluid Mechanics, vol. 812, pp. 199-221, February 2017.

[4] D. J. Tritton, "Experiments on the Flow Past a Circular Cylinder at Low Reynolds Numbers," Journal of Fluid Mechanics, vol. 6, no. 4, pp. 547-567, November 1959.

[5] S. Taneda, "Experimental Investigation of Vortex Streets," Journal of the Physical Society of Japan, vol. 20, no. 9, pp. 1714-1721, June 1965.

[6] M. Nishioka and H. Sato, "Measurements of Velocity Distributions in the Wake of a Circular Cylinder at Low Reynolds Numbers," Journal of Fluid Mechanics, vol. 65, no. 1, pp. 97-112, August 1974.

[7] M. Braza, P. Chassaing, and H. H. Minh, "Prediction of Large-Scale Transition Features in the Wake of a Circular Cylinder," Physics of Fluids A: Fluid Dynamics, vol. 2, no. 8, pp. 1461-1471, August 1990.

[8] R. Franke, W. Rodi, and B. Schönung, "Numerical Calculation of Laminar Vortex-Shedding Flow Past Cylinders," Journal of Wind Engineering and Industrial Aerodynamics, vol. 35, pp. 237-257, 1990.

[9] F. Ohle and H. Eckelmann, "Modeling of a von Kármán Vortex Street at Low Reynolds Numbers," Physics of Fluids A: Fluid Dynamics, vol. 4, no. 8, pp. 1707-1714, August 1992.

[10] Z. Huang, J. A. Olson, R. J. Kerekes, and S. I. Green, "Numerical Simulation of the Flow around Rows of Cylinders," Computers & Fluids, vol. 35, no. 5, pp. 485-491, June 2006.

[11] O. Posdziech and R. Grundmann, "A Systematic Approach to the Numerical Calculation of Fundamental Quantities of the Two-Dimensional Flow over a Circular Cylinder," Journal of Fluids and Structures, vol. 23, no. 3, pp. 479-499, April 2007.

[12] L. Qu, C. Norberg, L. Davidson, S. H. Peng, and F. Wang, "Quantitative Numerical Analysis of Flow Past a Circular Cylinder at Reynolds Number between 50 and 200," Journal of Fluids and Structures, vol. 39, pp. 347-370, May 2013.

[13] J. Ito and H. Niino, "Atmospheric Kármán Vortex Shedding from Jeju Island, East China Sea: A Numerical Study," Monthly Weather Review, vol. 144, no. 1, pp. 139-148, January 2016.

[14] N. S. Raghavendra, V. K. Tushar, S. S. Vivek, N. Sohail, and S. Sanketh, "Simulation of Kármán Vortex Street of Bluff Bodies for Piezoelectric Energy Harvesters," International Journal for Research in Applied Science & Engineering Technology, vol. 8, no. V, pp. 1959-1964, May 2020.

[15] U. Ali, M. D. Islam, and I. Janajreh, "Flow over Rotationally Oscillating Heated Circular Cylinder at Low Reynolds Number," Ocean Engineering, vol. 265, article no. 112515, December 2022.

[16] M. M. Zdravkovich, Flow around Circular Cylinders: Vol. 1: Fundamentals, Oxford: Oxford University Press, 1997.

[17] M. M. Zdravkovich, Flow around Circular Cylinders: Vol. 2: Applications, Oxford: Oxford University Press, 2003.

[18] A. Kozelkov, A. Kurkin, A. Korotkov, S. Lashkin, and E. Lashkina, "Three-Dimensional Simulations of Viscous Incompressible Fluid Flows on Grids with Unmatched Grid Interfaces," Fluids, vol. 7, no. 11, article no. 346, November 2022.

[19] J. Li, X. Lin, and Z. Chen, Finite Volume Methods for the Incompressible Navier-Stokes Equations, Cham Springer, 2022.

[20] D. G. Roychowdhury, Computational Fluid Dynamics for Incompressible Flows, 1st ed., Boca Raton, Florida: CRC Press, 2020.

[21] C. Ai, Y. Ma, C. Yuan, Z. Xie, G. Dong, and T. Stoesser, "Vortex Shedding and Evolution Induced by the Interactions between a Solitary Wave and a Submerged Horizontal Plate," Journal of Hydraulic Research, vol. 60, no. 2, pp. 311-325, 2022.

[22] J. Chang, Q. Zhang, L. He, and Y. Zhou, "Shedding Vortex Characteristics Analysis of NACA 0012 Airfoil at Low Reynolds Numbers," Energy Reports, vol. 8, no. 4, pp. 156-174, July 2022.

[23] X. Li, Z. Li, B. Liu, J. Zhang, and W. Zhu, "Numerical Research on a Vortex Shedding induced Piezoelectric-electromagnetic Energy Harvester," Journal of Intelligent Material Systems and Structures, vol. 33, no. 1, pp. 105-120, 2021.

[24] S. J. Liang, J. H. Tang, and M. S. Wu, "Solution of Shallow-Water Equations Using Least-Squares Finite-Element Method," Acta Mechanica Sinica, vol. 24, no. 5, pp. 523-532, October 2008.

[25] S. J. Liang and T. W. Hsu, "Least-Squares Finite-Element Method for Shallow-Water Equations with Source Terms," Acta Mechanica Sinica, vol. 25, no. 5, pp. 597-610, October 2009.

[26] S. J. Liang, C. C. Young, C. Dai, N. J. Wu, and T. W. Hsu, "Simulation of Ocean Circulation of Dongsha Water Using Non-Hydrostatic Shallow-Water Model," Water, vol. 12, no. 10, article no. 2832, October 2020.

[27] B. N. Jiang, The Least-Squares Finite Element Method: Theory and Applications in Computational Fluid Dynamics and Electromagnetics, Berlin: Springer, 1998.

[28] M. D. Gunzburger, Finite Element Methods for Viscous Incompressible Flows: A Guide to Theory Practice and Algorithms, Boston: Academic Press, 1989.

[29] G. F. Carey and B. N. Jiang, "Element-by-Element Linear and Nonlinear Solution Schemes," Communications in Applied Numerical Methods, vol. 2, no. 2, pp. 145-153, March/April 1986.

[30] U. Fey, M. König, and H. Eckelmann, "A New Strouhal–Reynolds-Number Relationship for the Circular Cylinder in the Range 47<Re<2×105," Physics of Fluids, vol. 10, no. 7, pp. 1547-1549, July 1998.